

# Bismuth Atom Tailoring of Indium Oxide Surface Frustrated Lewis Pairs Boosts Heterogeneous CO<sub>2</sub> Photocatalytic Hydrogenation

**Tingjiang Yan**

Qufu Normal University

**Na Li**

Qufu Normal University

**Linlin Wang**

Qufu Normal University

**Weiguang Ran**

Qufu Normal University

**Paul Duchesne**

University of Toronto

**Lili Wan**

Nankai University

**Nhat Truong Nguyen**

University of Toronto <https://orcid.org/0000-0002-7651-3174>

**Lu Wang**

University of Toronto

**Meikun Xia**

University of Toronto

**Geoffrey Ozin** (✉ [g.ozin@utoronto.ca](mailto:g.ozin@utoronto.ca))

University of Toronto <https://orcid.org/0000-0002-6315-0925>

---

## Article

**Keywords:** CO<sub>2</sub> photocatalysis, surface frustrated Lewis pairs, Bismuth atom, Bi<sub>3</sub>, In<sub>3+</sub> ions

**Posted Date:** August 4th, 2020

**DOI:** <https://doi.org/10.21203/rs.3.rs-49848/v1>

**License:**   This work is licensed under a Creative Commons Attribution 4.0 International License.

[Read Full License](#)

**Version of Record:** A version of this preprint was published at Nature Communications on November 30th, 2020. See the published version at <https://doi.org/10.1038/s41467-020-19997-y>.

# Abstract

The surface frustrated Lewis pairs (SFLPs) on defect-laden metal oxides provide catalytic sites to activate H<sub>2</sub> and CO<sub>2</sub> molecules and enable efficient gas-phase CO<sub>2</sub> photocatalysis. Lattice engineering of metal oxides provides a useful strategy to tailor the reactivity of SFLPs. Herein a one-step solvothermal synthesis is developed that enables isomorphic replacement of In<sup>3+</sup> ions in UV-absorbing In<sub>2</sub>O<sub>3</sub> by single-site Bi<sup>3+</sup> ions to generate a new class of full-spectrum UV-Vis-NIR absorbing BiIn<sub>2-x</sub>O<sub>3</sub> materials. Through compositional tuning, these materials prove to be three orders of magnitude more photoactive for the reverse water gas shift reaction (i.e., CO<sub>2</sub> + H<sub>2</sub> → CO + H<sub>2</sub>O) than In<sub>2</sub>O<sub>3</sub> itself, while also exhibiting notable photoactivity towards methanol production from carbon dioxide (i.e., CO<sub>2</sub> + 3H<sub>2</sub> → CH<sub>3</sub>OH + H<sub>2</sub>O). The defective form of In<sub>2</sub>O<sub>3</sub> containing oxygen vacancy sites can create SFLPs involving In<sup>3+</sup> nearby the oxygen vacancy, which function as Lewis acidic sites, while lattice oxide O<sup>2-</sup> act as Lewis basic sites. In this study, it is discovered that the reactivity of these SFLPs can be further enhanced by single-site Bi<sup>3+</sup> ion isomorphic substitution of Lewis acidic site In<sup>3+</sup>, thereby enhancing the propensity to activate CO<sub>2</sub> molecules. In addition, the increased solar absorption efficiency and efficient charge separation and transfer of BiIn<sub>2-x</sub>O<sub>3</sub> also contribute to the improved photocatalytic performance. These traits lead to enhanced binding and activation of CO<sub>2</sub>, exemplifying the opportunities that exist for atom-scale engineering in heterogeneous CO<sub>2</sub> photocatalysis, another step towards the vision of the solar CO<sub>2</sub> refinery.

# Background

The increasing energy demands of civil society have accelerated the consumption of coal, oil and natural gas and associated greenhouse gas emissions. This situation is tipping the delicate balance of CO<sub>2</sub> in our atmosphere leading to global warming. To this end, the photocatalytic hydrogenation of CO<sub>2</sub> into value-added chemicals and fuels has attracted global attention, touted a promising means of achieving a carbon-neutral economy<sup>1-3</sup>. Although materials such as Pd/Nb<sub>2</sub>O<sub>5</sub><sup>4</sup>, Ru/Al<sub>2</sub>O<sub>3</sub><sup>5</sup>, LDH nanosheets<sup>6</sup> and Co-PS@SiO<sub>2</sub><sup>7</sup> have been successfully employed as photocatalysts for CO<sub>2</sub> hydrogenation, a photocatalyst does not currently exist that can meet all the stringent requirements for practical application, including a broad solar response, high conversion efficiency, robust stability and low cost. This renders the design of a practical photocatalyst for CO<sub>2</sub> hydrogenation a challenge.

Besides catalyst modifications designed to broaden spectral response and improve charge transfer efficiency, it is also important to accelerate conversion rates of H<sub>2</sub> or CO<sub>2</sub> on specially designed surface sites to boost photon and energy efficiency. Recently, surface frustrated Lewis pairs (SFLPs) have shown a propensity towards H<sub>2</sub> dissociation and CO<sub>2</sub> activation, a key enabler for many catalytic reactions, including hydrogenation, hydroamination and CO<sub>2</sub> reduction<sup>8-10</sup>. Generally speaking, SFLPs comprise proximal Lewis acidic and Lewis basic sites providing synergetic activation of reactant molecules. For example, SFLPs sites in the In<sub>2</sub>O<sub>3-x</sub>(OH)<sub>y</sub> photocatalyst, comprised of a coordinately unsaturated Lewis acidic In atom, proximal to an oxygen vacancy and an adjacent Lewis basic hydroxide group, enable the

heterolysis of  $H_2$  and reaction with  $CO_2$  to form either  $CO$  or  $CH_3OH$ <sup>11-13</sup>. As well, SFLPs involving coordinately unsaturated surface cobalt sites adjacent to surface hydroxides in the  $CoGeO_2(OH)_2$  photocatalyst form  $CH_4$  from  $H_2O$  and  $CO_2$ <sup>14</sup>. In addition, SFLPs in oxygen vacancy laden  $CeO_2$  bearing SFLPs catalyze the hydrogenation of alkenes and alkynes<sup>15</sup>. All of these cases utilize oxygen vacancies and hydroxides to engineer the catalytic activity of SFLPs. How to tailor the reactivity of the SFLPs themselves is rarely mentioned.

Indium sesquioxide ( $In_2O_3$ ) is proving to be a promising catalyst for the thermal hydrogenation of  $CO_2$  to  $CH_3OH$  or  $CO$ <sup>16-18</sup>. Experimental and computational studies of  $CO_2$  hydrogenation over oxygen vacancy laden  $In_2O_3$  revealed that methanol formation was favored over the reverse water gas shift (RWGS) reaction<sup>19,20</sup>. Methanol production was remarkably enhanced when  $In_2O_3$  was supported on  $ZrO_2$  arising from electronic support effects<sup>21</sup>. A bifunctional catalyst composed of partially reduced  $In_2O_3$  supported on HZSM-5 could convert  $CO_2$  directly into gasoline-range hydrocarbons with a 78.6% selectivity due to the synergistic effects of these two components<sup>22</sup>. By controlling the degree of non-stoichiometry in  $In_2O_{3-x}$ , a black indium oxide catalyst, which utilized the entire solar spectrum, facilitated the photothermal RWGS reaction under ambient conditions with 100% selectivity<sup>23</sup>. Tailoring the electronic properties of  $In_2O_3$  can also be achieved via replacement of an indium atom in the lattice with a  $H_2$  spillover palladium atom, although the rarity and cost of palladium could prove an issue for its practical implementation<sup>24</sup>.

Bismuth, regarded as a 'green' element, has a long and fascinating history<sup>25</sup>. The Incas in sixteenth century South America, made corrosion resistant bronzes for their knives by mixing bismuth with tin<sup>26</sup>. Paracelsus in fifteenth century Germany, recognized bismuth as a non-toxic brother to lead<sup>27</sup>. Since, it is finding myriad eco-friendly uses from cosmetics and personal care products to medicine and lubricants. Most recently it has proved to be a serious contender for replacing toxic lead halide perovskite materials in solar cells with non-toxic bismuth oxyiodide, retaining a comparable energy conversion efficiency of 22%<sup>28</sup>. Contextually, bismuth materials with layered structures and visible light absorption properties, exemplified by  $BiOX$  ( $X=Cl, Br, I$ ),  $Bi_2MO_6$  ( $M=Mo, W$ ),  $BiVO_4$  and  $Bi_2S_3$ , behave as photocatalysts to be applied in dye degradation, water and carbon dioxide reduction<sup>29</sup>.

Described herein, we developed a facile solvothermal route to achieve atom-precise substitution of  $Bi^{3+}$  for  $In^{3+}$  sites in  $In_2O_3$  and realize the tailor of the reactivity of SFLPs as well as the electronic properties of  $In_2O_3$ . To amplify, by substituting cheaper and safer bismuth for indium in UV absorbing  $In_2O_3$ , one can create the full-spectrum UV-Vis-NIR light absorber  $Bi_xIn_{2-x}O_3$ . Significantly, single-site  $Bi^{3+}$  substitution for  $In^{3+}$  provides strong Lewis acidic/basic  $Bi^{3+}-O^{2-}$  pairs that enhance  $CO_2$  adsorption and activation, while Bi  $6s^2$  lone-pair electrons create mid-gap energy states. Atom-precise lattice engineering of this kind, boosts the reactivity of SFLPs and the harvesting efficiency of solar photons by  $Bi_xIn_{2-x}O_3$  compared to

$\text{In}_2\text{O}_3$ , which enables 1,000 times photoactivity enhancement of the RWGS reaction together with a noticeable increase in the production of solar methanol.

## Results

**Structural characterizations of single-site  $\text{Bi}_x\text{In}_{2-x}\text{O}_3$ .**  $\text{Bi}_x\text{In}_{2-x}\text{O}_3$  nanocrystals were prepared *via* a one-step solvothermal route, in which the molar ratio of Bi could be controlled by adjusting the concentration of  $\text{Bi}(\text{NO}_3)_3$  and  $\text{In}(\text{NO}_3)_3$  precursors. The mole percent Bi content of each sample in the  $\text{Bi}_x\text{In}_{2-x}\text{O}_3$  series of nanocrystals was determined using inductively coupled plasma mass spectrometry (ICP-MS, Supplementary Table 1). Transmission electron microscopy (TEM) shows that the pristine  $\text{In}_2\text{O}_3$  nanocrystals are flower-like agglomerates of small nanocrystals with an average size of 3.7 nm (Supplementary Fig. 1).  $\text{Bi}^{3+}$  substitution results in similarly sized  $\text{Bi}_x\text{In}_{2-x}\text{O}_3$  nanocrystals (3.5 nm) that show lattice fringes with a spacing of 2.92 Å, corresponding to the (222) plane of bcc  $\text{In}_2\text{O}_3$  (Supplementary Fig. 2). The obtained SAED pattern shown no evidence of any metallic Bi or  $\text{Bi}_2\text{O}_3$ . Most significantly, spherical aberration-corrected scanning transmission electron microscopy (STEM) images provide an insightful and distinct result, in which atomically dispersed single-site Bi atoms are revealed under these high-resolution imaging conditions as bright dots (Fig. 1a and 1b). Energy-dispersive X-ray spectroscopy (EDS) line scans and elemental mapping (Fig. 1c and Supplementary Fig. 3) provided further evidence for the homogeneous distribution of elemental Bi in these  $\text{Bi}_x\text{In}_{2-x}\text{O}_3$  nanocrystals.

The phase structure of the obtained  $\text{Bi}_x\text{In}_{2-x}\text{O}_3$  nanocrystals was studied by powder X-ray diffraction (PXRD, Fig. 1d). All the  $\text{Bi}_x\text{In}_{2-x}\text{O}_3$  nanocrystals displayed nearly identical XRD patterns diagnostic of face-centered cubic  $\text{In}_2\text{O}_3$  except that the diffraction peaks were shifted to lower  $2\theta$  values relative to those of pristine  $\text{In}_2\text{O}_3$ . This result indicates  $\text{In}^{3+}$  were isomorphously substituted by  $\text{Bi}^{3+}$  which has a larger ionic radius than  $\text{In}^{3+}$  (*i.e.*, 0.96 Å *versus* 0.81 Å). This conclusion is supported by the In 3d peaks in the corresponding X-ray photoelectron spectroscopy (XPS) spectra (Supplementary Fig. 4a), which exhibited a gradual positive energy shift for  $\text{Bi}_x\text{In}_{2-x}\text{O}_3$  nanocrystals relative to pure  $\text{In}_2\text{O}_3$ , that is attributed to the higher electronegativity of  $\text{Bi}^{3+}$  compared to  $\text{In}^{3+}$ . The spin-orbit coupled doublet of Bi 4f XPS peaks at 158.6 eV and 163.9 eV define the oxidation state of bismuth as  $\text{Bi}^{3+}$  rather than  $\text{Bi}^0$  (Supplementary Fig. 4b), following the isomorphous substitution of  $\text{In}^{3+}$  by  $\text{Bi}^{3+}$ . The electron paramagnetic resonance (EPR) spectra of  $\text{Bi}_x\text{In}_{2-x}\text{O}_3$  nanocrystals at both room temperature and 77 K revealed the absence of paramagnetic species, thereby providing further evidence for the lack of  $\text{Bi}^0$  (Supplementary Fig. 5).

Synchrotron radiation-based X-ray absorption spectroscopy (XAS) was further used to obtain information regarding the local structural environment of these distributed Bi sites. The Bi  $L_3$ -edge X-ray absorption near-edge structure (XANES) spectra in Fig. 1e reveal visible similarities between the 1.0% and 5.0%  $\text{Bi}_x\text{In}_{2-x}\text{O}_3$  sample spectra and that of the  $\text{Bi}_2\text{O}_3$  reference. These similarity are to be expected, given that Bi atoms in both  $\text{Bi}_2\text{O}_3$  and  $\text{Bi}_x\text{In}_{2-x}\text{O}_3$  lattices are expected to be octahedrally coordinated by oxygen atoms, leading to similarities in their structural and electronic properties. The Fourier-transformed Bi  $L_3$ -

edge extended X-ray absorption fine structure (EXAFS) spectra are presented in Fig. 1f. The similar positions of the Bi–O peak positions suggest that these bond lengths in the  $\text{Bi}_x\text{In}_{2-x}\text{O}_3$  samples are similar to those in the  $\text{Bi}_2\text{O}_3$  reference. In stark contrast, though, the observed Bi–M peaks appear at distinctly different positions in the  $\text{Bi}_x\text{In}_{2-x}\text{O}_3$  spectra, revealing a distinct structural difference relative to the  $\text{Bi}_2\text{O}_3$  reference. In order to more accurately quantify these differences in bond length and structure, the spectra were also fitted to extract key structural parameter values (Supplementary Fig. 6 and Supplementary Table 2). The resulting Bi–In bond lengths in the  $\text{Bi}_x\text{In}_{2-x}\text{O}_3$  samples are shorter than those found in the pristine  $\text{Bi}_2\text{O}_3$  lattice, though slightly longer than those observed in the pristine  $\text{In}_2\text{O}_3$  lattice. Relatively larger Debye-Waller coefficient values for the Bi–O peaks in  $\text{Bi}_x\text{In}_{2-x}\text{O}_3$  samples were also observed, reflecting a broader range of constituent Bi–O bond lengths.

**CO<sub>2</sub> hydrogenation performance.** The photocatalytic CO<sub>2</sub> hydrogenation activity of  $\text{Bi}_x\text{In}_{2-x}\text{O}_3$  nanocrystals was evaluated in a batch reactor under simulated solar light irradiation and using a 1:1 ratio of CO<sub>2</sub> and H<sub>2</sub> gases. In these experiments, the RWGS reaction (*i.e.*,  $\text{CO}_2 + \text{H}_2 \rightarrow \text{CO} + \text{H}_2\text{O}$ ) led to CO being the sole product detected. The CO production rates revealed that 1.0%  $\text{Bi}_x\text{In}_{2-x}\text{O}_3$  was more active than  $\text{In}_2\text{O}_3$  by approximately three orders of magnitude (Fig. 2a), with an impressive peak rate of 8000 mmol g<sup>-1</sup> h<sup>-1</sup> for its first run, as compared to just 35 mmol g<sup>-1</sup> h<sup>-1</sup> for pristine  $\text{In}_2\text{O}_3$ . The estimated turnover frequency (TOF) of  $\text{In}_2\text{O}_3$  and 1.0%  $\text{Bi}_x\text{In}_{2-x}\text{O}_3$  is 0.42 h<sup>-1</sup> and 93.6 h<sup>-1</sup>, respectively (Supplementary Note 1), implying that substituting Bi atoms into  $\text{In}_2\text{O}_3$  nanocrystals significantly enhanced the photocatalytic activity towards CO<sub>2</sub> hydrogenation. Remarkably, this boost in catalytic activity was much more dramatic than that observed in analogous hydroxylated systems (*i.e.*,  $\text{Bi}_x\text{In}_{2-x}\text{O}_3(\text{OH})_y$ )<sup>30</sup>, thereby suggesting a distinct and potent mechanism of catalytic activity enhancement in  $\text{Bi}_x\text{In}_{2-x}\text{O}_3$ . Furthermore, such a CO production rate is much higher than some of the most active noble metal decorated photocatalysts (Supplementary Table 3). In addition, the 1.0%  $\text{Bi}_x\text{In}_{2-x}\text{O}_3$  was very stable, exhibiting a CO production rate that was still roughly 600 times greater than the 11 mmol g<sup>-1</sup> h<sup>-1</sup> exhibited by pristine  $\text{In}_2\text{O}_3$  under the same experimental conditions. In both cases, the CO production rate was observed to decrease over the course of five consecutive runs.

The actual bulk reaction temperature for  $\text{In}_2\text{O}_3$  and  $\text{Bi}_x\text{In}_{2-x}\text{O}_3$  tested by IR camera is about 70 and 115 °C (Supplementary Fig. 7), respectively. The relatively low thermal energy supplied by solar light indicates the limited contribution of photothermal effect on the photocatalytic RWGS reaction. As an endothermic reaction, the rate of the RWGS is expected increase quite rapidly as a function of temperature. According to the Arrhenius Law, the rate should approximately double for every 10 °C increase in temperature. Thus, we would expect the reaction rate to increase by a factor of approximately 22.5, assuming that the bulk temperature of the catalyst accurately reflects the temperature of the catalytically active sites. Based on the rate of pristine  $\text{In}_2\text{O}_3$  (*i.e.*, 35 mmol g<sup>-1</sup> h<sup>-1</sup>), this would result in a rate increase to about 788 mmol g<sup>-1</sup> h<sup>-1</sup> and account for about 10 % of the observed activity increase, thereby suggesting the existence of a significant photochemical effect. Notably, the marked increase in CO production rate upon substituting

single-site Bi atoms into  $\text{In}_2\text{O}_3$  was highly dependent on the concentration of Bi atoms (Fig. 2b). Meanwhile, isotopically labelled  $^{13}\text{CO}_2$  experiment confirmed that CO was the unequivocal product from photocatalytic  $\text{CO}_2$  hydrogenation (Fig. 2c).

We also investigated the dependence of the CO production rate on the wavelength of light, to demonstrate the  $\text{CO}_2$  hydrogenation proceeds mainly through a photocatalytic process. As seen in the action spectra shown in Fig. 2d and Supplementary Fig. 8, the production rate of CO monotonically decreased with longer wavelengths of the light, which correlates with the optical absorption spectrum of pristine  $\text{In}_2\text{O}_3$  and  $\text{Bi}_x\text{In}_{2-x}\text{O}_3$  catalysts. It should also be mentioned that the CO production rate remained at about  $2000 \text{ mmol g}^{-1} \text{ h}^{-1}$  on 1.0%  $\text{Bi}_x\text{In}_{2-x}\text{O}_3$ , even when a 500 nm cut-off filter was applied, thus implying that  $\text{Bi}_x\text{In}_{2-x}\text{O}_3$  nanocrystals can function as broadband, green photocatalysis for harvesting solar energy.

In light of the promising performance of  $\text{Bi}_x\text{In}_{2-x}\text{O}_3$  nanocrystals towards gas-phase  $\text{CO}_2$  hydrogenation, this new catalyst was also studied for solar methanol production in a flow reactor at  $230^\circ\text{C}$ , both with and without light irradiation. As shown in Supplementary Fig. 9, all catalysts exhibited similarly low CO and  $\text{CH}_3\text{OH}$  production rates under purely thermal conditions; however, a remarkable enhancement in the production rates of CO and  $\text{CH}_3\text{OH}$  was obtained on changing from dark to light conditions. In this case, pristine  $\text{In}_2\text{O}_3$  exhibited CO and  $\text{CH}_3\text{OH}$  production rates of  $312$  and  $82 \text{ mmol g}^{-1} \text{ h}^{-1}$ , respectively (Fig. 3a and 3b). In comparison, the single-site  $\text{Bi}_x\text{In}_{2-x}\text{O}_3$  samples exhibited much better activities for both CO and  $\text{CH}_3\text{OH}$  production, with 1.0%  $\text{Bi}_x\text{In}_{2-x}\text{O}_3$  exhibiting the highest CO and  $\text{CH}_3\text{OH}$  production rates of  $918 \text{ mmol g}^{-1} \text{ h}^{-1}$  and  $158 \text{ mmol g}^{-1} \text{ h}^{-1}$ , respectively. Overall, the measured activities of the  $\text{Bi}_x\text{In}_{2-x}\text{O}_3$  samples were highly dependent on Bi content and showed a volcano-shaped trend. The volcano trend of the activity towards  $\text{CO}_2$  hydrogenation *versus* the extent of  $\text{In}^{3+}$  substitution by the larger, more electronegative,  $6s^2$  stereochemically active lone-pair containing  $\text{Bi}^{3+}$ , can be attributed to a subtle interplay of numerous and competing intertwined properties: chemical effects (*e.g.*, influence of surface Lewis acidity and basicity of In-O-In, In-O-Bi, Bi-O-Bi sites on  $\text{CO}_2\text{-H}_2$  adsorption, activation, reaction processes) and physical effects (*e.g.*, photogenerated electron and hole charge-separation and charge-trapping by bismuth and oxygen vacancy mid gap states).

The  $\text{CH}_3\text{OH}$  and CO production rates of  $\text{Bi}_x\text{In}_{2-x}\text{O}_3$  nanocrystals showed negligible deactivation, even after 50 h of continuous testing under light irradiation at  $230^\circ\text{C}$  (Supplementary Fig. 10a), suggesting their excellent catalytic stability. The recorded XRD patterns, TEM images and XPS spectra (Supplementary Fig. 10b-d) for the spent  $\text{Bi}_x\text{In}_{2-x}\text{O}_3$  photocatalysts after 50 h of reaction demonstrate that, except for a slight increase in particle size, the phase and oxidation states of the nanocrystals were well maintained, confirming their favourable structural stability.

To obtain more information on the origin of the activity enhancement under flow reaction conditions, activity tests were also conducted at lower reaction temperatures, beginning where products can be

observed (130, 195 and 210 °C), with and without light irradiation (Supplementary Fig. 11). The drastic activity difference between dark and light conditions lend further support confirmed the contribution of the photochemical effect on CO and CH<sub>3</sub>OH production. Moreover, based on the Arrhenius plots for 1.0% Bi<sub>x</sub>In<sub>2-x</sub>O<sub>3</sub>, the apparent activation energy for the CO and CH<sub>3</sub>OH photochemical processes are much lower than the thermochemical ones (Fig. 3c and 3d), reflecting the solar advantage for the excited-state reaction pathway relative to the ground state pathway<sup>31</sup>.

**Photocatalytic reaction pathway.** The photocatalytic CO<sub>2</sub> hydrogenation reaction involves photon-absorption, electron-hole separation, and CO<sub>2</sub> adsorption/activation processes. The first two steps are closely related to the intrinsic nature of the photocatalyst, while the third is highly dependent on the gas-solid interface. A significant red shift occurs in the absorption edge of UV-visible-NIR spectra (Fig. 4a), along with a broad absorption band in the spectral range of 400 to 800 nm, which grows with Bi<sup>3+</sup> content and is accompanied by a change in color from cream to rust (Supplementary Fig. 12). Corresponding electronic band gaps of Bi<sub>x</sub>In<sub>2-x</sub>O<sub>3</sub> reduce gradually from 2.77 to 2.45, 1.99, 1.46 and 1.27 eV as a result of Bi<sup>3+</sup> substitution (Supplementary Fig. 13). This is consistent with the simulated band structures that show the introduction of Bi can decrease the band gap of In<sub>2</sub>O<sub>3</sub> (Fig. 4b and 4c). The total density of states (DOS) and partial density of states (PDOS) (Supplementary Fig. 14) can further reveal that the substitution of Bi at the In site induces mid-gap energy states with Bi 6s states below the conduction band edge of In<sub>2</sub>O<sub>3</sub> and is consistent with the reported results in this paper<sup>32-34</sup>.

To understand the photogenerated charge transfer mechanism, the room temperature photoluminescence (PL) spectra of pristine In<sub>2</sub>O<sub>3</sub> and 1.0% Bi<sub>x</sub>In<sub>2-x</sub>O<sub>3</sub> nanocrystals are shown in Fig. 4d. The pristine In<sub>2</sub>O<sub>3</sub> nanocrystals exhibited a strong green emission peak centered at ca. 440 nm, originating from the radiative recombination of photo-excited electrons trapped in mid-gap oxygen vacancy states with photogenerated holes in the valence band<sup>35</sup>. The existence of oxygen vacancies is further evidenced by the O 1s core level XPS spectra (Supplementary Fig. 15). In contrast, the incorporation of single-site Bi into In<sub>2</sub>O<sub>3</sub> leads to weakening and broadening of the PL emission peak. This can be explained in two ways. One is that the substitutional Bi<sup>3+</sup> slightly decreases the concentration of oxygen vacancies (Supplementary Fig. 16), which would decrease the intensity due to electron-hole radiative recombination. Alternatively, the substituted Bi<sup>3+</sup> states lying below the conduction band of In<sub>2</sub>O<sub>3</sub> could also act as traps capturing photo-excited electrons and inhibiting electron-hole recombination emission, resulting in lower PL emission. Thus, as illustrated in Fig. 4e, the substituted Bi<sup>3+</sup> sites (denoted as Bi'), oxygen vacancies [O], coordinately unsaturated indium In' sites and oxygen O' sites, exist as mid-gap defect states (comprising surface frustrated Lewis pairs, SFLPs) in the bandgap of Bi<sub>x</sub>In<sub>2-x</sub>O<sub>3</sub>, can function as traps for photogenerated electrons and holes enabling the reaction between CO<sub>2</sub>/H<sub>2</sub><sup>36,37</sup>. This results in the quenching of steady-state PL emission as well as a slight shortening of the average fluorescence lifetime from 120 to 110 ps, probed by time-resolved PL spectroscopy (Supplementary Fig. 17). Albeit small, this reduction of the fluorescence lifetime, suggests that, relative to In<sub>2</sub>O<sub>3</sub>, single-site Bi atoms can increase the occurrence of competitive non-radiative relaxation processes in Bi<sub>x</sub>In<sub>2-x</sub>O<sub>3</sub><sup>38-40</sup>.

Apart from its effect on the electronic structure and charge transfer, single-site  $\text{Bi}^{3+}$  substitution is also expected to strengthen the adsorption-bonding-activating ability of  $\text{Bi}_x\text{In}_{2-x}\text{O}_3$  toward  $\text{CO}_2$ . The surface area can be excluded as it maintains in the range of  $32\sim 34\text{ m}^2\text{ g}^{-1}$  for the catalysts (Supplementary Table 4). With respect to the surface chemistry,  $\text{CO}_2$  can bond through its carbon atom and oxygen atoms to either the surface oxygen atoms, metal sites, or directly with the oxygen vacancies of metal oxides (Supplementary Fig. 18)<sup>41-43</sup>. To investigate the effect of  $\text{Bi}^{3+}$  substitution on the interaction between  $\text{CO}_2$  and  $\text{Bi}_x\text{In}_{2-x}\text{O}_3$  or pristine  $\text{In}_2\text{O}_3$  nanocrystals,  $\text{CO}_2$  temperature-programmed desorption ( $\text{CO}_2$ -TPD) measurements were initially performed. As shown in Fig. 5a, one broad desorption peak at around  $100\text{ }^\circ\text{C}$ , corresponding to physically adsorbed  $\text{CO}_2$ , is observed for all  $\text{Bi}_x\text{In}_{2-x}\text{O}_3$  nanocrystals and pristine  $\text{In}_2\text{O}_3$ . A significant desorption peak is clearly observed at  $256\text{ }^\circ\text{C}$  for pristine  $\text{In}_2\text{O}_3$  and can be attributed to the chemical desorption of  $\text{CO}_2$  that is binding with oxygen vacancies to form bent  $\text{CO}_2^{\text{d}}$  species<sup>44</sup>. Since  $\text{Bi}^{3+}$  substitution results in fewer oxygen vacancies, this peak intensity gradually decreases with increased  $\text{Bi}^{3+}$  doping of  $\text{Bi}_x\text{In}_{2-x}\text{O}_3$  nanocrystals and shifts slightly to higher temperatures (as high as  $275\text{ }^\circ\text{C}$  for 5.0 %  $\text{Bi}_x\text{In}_{2-x}\text{O}_3$ ), implying that the binding strength of  $\text{CO}_2$  and oxygen vacancies is remarkably enhanced. Moreover, weak desorption peaks at higher temperatures ( $300$  to  $600\text{ }^\circ\text{C}$ ) were clearly observed for  $\text{In}_2\text{O}_3$ , and can be assigned to the decomposition of surface  $\text{HCO}_3^-$  and  $\text{CO}_3^{2-}$  species<sup>45</sup>. After single-site  $\text{Bi}^{3+}$  substitution, typical desorption peaks can also be clearly identified and show a slight shift to higher temperatures, again indicating that these surface species are binding more strongly to the surface.

*In-situ* diffuse reflectance infrared Fourier-transform spectroscopy (DRIFTS) experiments were further carried out to identify surface species. Fig. 5b show the transient evolution of the surface species during  $\text{CO}_2$  adsorption over 1.0%  $\text{Bi}_x\text{In}_{2-x}\text{O}_3$  nanocrystals. The bands at  $1510$  and  $1372\text{ cm}^{-1}$  are assigned to the asymmetric and symmetric OCO stretching modes of monodentate carbonates ( $m\text{-CO}_3^{2-}$ ). The features at  $1549$  and  $1330\text{ cm}^{-1}$  are attributed to the asymmetric and symmetric OCO stretching modes of bidentate carbonates ( $b\text{-CO}_3^{2-}$ ). The bent  $\text{CO}_2^{\text{d}}$  species adsorbed at oxygen vacancy sites can be identified by two bands at  $1596$  and  $1348\text{ cm}^{-1}$ , corresponding to the asymmetric and symmetric stretching modes, respectively. The appearance of bands at  $1625$ ,  $1437$ ,  $1390$  and  $1222\text{ cm}^{-1}$  indicates the formation of bicarbonate species ( $\text{HCO}_3^-$ ). Moreover, a small amount of a linearly-adsorbed  $\text{CO}_2$  species with bands appearing between  $1000$  and  $1100\text{ cm}^{-1}$  can also be observed. Thus, via DRIFTS measurements, all the surface species observed during  $\text{CO}_2$ -TPD measurements,  $\text{CO}_3^{2-}$ ,  $\text{HCO}_3^-$  and  $\text{CO}_2^{\text{d}}$ , were observed and identified on  $\text{Bi}_x\text{In}_{2-x}\text{O}_3$  nanocrystals. All these surface species can be observed on pristine  $\text{In}_2\text{O}_3$ ; however, the peak intensities of these species are weaker than that on  $\text{Bi}_x\text{In}_{2-x}\text{O}_3$  nanocrystals, suggesting the improved  $\text{CO}_2$  adsorption-bonding-activating capacity after  $\text{Bi}^{3+}$  substitution.

Density functional theory (DFT) slab calculations were further carried out to unravel the promotion effect of  $\text{Bi}^{3+}$  substitution on  $\text{In}_2\text{O}_3$ . The perfect  $\text{In}_2\text{O}_3$  (110) surface was initially selected as it has proven to be

most thermodynamically stable<sup>20,46</sup>. The defective  $\text{In}_2\text{O}_3$  (110) surface with an oxygen vacancy at the  $\text{O}_4$  site was then created owing to the more favorable ability for  $\text{CO}_2$  activation and hydrogenation<sup>19</sup>. Following then, we examined the possibility of  $\text{Bi}^{3+}$  substitution at the In site.

As shown in Fig. 6a, the perfect  $\text{In}_2\text{O}_3$  (110) surface consists of chains of In and O atoms, with the numbering In and O atoms along the chain as repeating unit. The surface In and O in the chain are adjacent and contiguous to each other, forming a classic Lewis acid-base adjunct, whereas the unbonded  $\text{In}_3$  and  $\text{In}_4$  in the chain and O in the top layer show a distance of 4.106 and 4.312 Å, respectively, which may deliver SFLPs-like activity (Fig. 6d). However, the electronic interactions between  $\text{In}_3$  or  $\text{In}_4$  and its neighbouring  $\text{O}_4$  will block the function of  $\text{In}_3\text{-O}$  or  $\text{In}_4\text{-O}$  pairs. Therefore, the removal of oxygen atom at the  $\text{O}_4$  site is the prerequisite to construct a pair of unbonded Lewis acid and base sites. When the  $\text{O}_4$  atom is removed, two In atoms ( $\text{In}_3$  and  $\text{In}_4$ ) are coordinatively unsaturated and one oxygen vacancy ( $\text{O}_{\text{V}4}$ ) is produced (Fig. 6b). However, in this case, only one In atom ( $\text{In}_4$ ) locates at the surface while the other one ( $\text{In}_3$ ) moves to the inner atomic layer. The surface  $\text{In}_4$  atom is found to be surrounded by two adjacent oxygen atoms, of which the  $\text{In}_4\text{-O}$  with a distance of 4.222 Å can construct a SFLPs site (Fig. 6e). We further investigated the effect of  $\text{Bi}^{3+}$  substitution at  $\text{In}_4$  site on the configuration and charge population (Fig. 6c and f). As compared to  $\text{In}_4\text{-O}$  configuration,  $\text{Bi}_4\text{-O}$  shows a shorter distance (3.821 Å) but can still fall in the domain of solid SFLPs. On the other hand, the Bader charge calculations show that the related Lewis acid  $\text{Bi}^{3+}$  and Lewis base  $\text{O}^{2-}$  involve atomic local charges of + 1.500 e and - 0.910 e, respectively, which is higher than that of the  $\text{In}^{3+}$  and  $\text{O}^{2-}$  pair (+ 1.300 e and - 0.900 e). The larger charge difference between the Lewis acid and Lewis base pairs in the  $\text{Bi}_x\text{In}_{2-x}\text{O}_3$  compared with that of defective  $\text{In}_2\text{O}_3$  would form more active Lewis acid-base pairs than the  $\text{In}_2\text{O}_3$  pair can muster, and therefore could deliver a higher capability to activate  $\text{CO}_2$  molecules, consistent well with the DRIFTS and  $\text{CO}_2$ -TPD results.

In the photo-excited state of a SFLPs system, the Lewis acidity and Lewis basicity have been shown to increase as compared with the ground state, thereby facilitating the photochemical  $\text{CO}_2$  hydrogenation, with a decrease in activation energy. To get more insight into the improved activity from  $\text{Bi}^{3+}$  substitution, *in-situ* DRIFTS experiments were further performed under reaction conditions to detect the reaction intermediates and uncover the photocatalytic pathway in the  $\text{CO}_2$  hydrogenation process. As shown in Fig. 5c, when the  $\text{Bi}_x\text{In}_{2-x}\text{O}_3$  nanocrystals were exposed to the mixture of  $\text{CO}_2$  and  $\text{H}_2$  gases, bidentate formate ( $^*\text{HCOO}$ ), methoxy ( $^*\text{H}_3\text{CO}$ ) and carboxylate ( $^*\text{CO}_2$ )<sup>47</sup>, were the three principal intermediates observed from the transformation of bicarbonate and carbonate species, as evidenced by the decrease and disappearance of characteristic bands at 1510, 1390 and 1222  $\text{cm}^{-1}$ . The  $^*\text{HCOO}$  species can be linked to fingerprint modes at 2973 and 2731  $\text{cm}^{-1}$ , which correspond to a combination of the CH bending and OCO stretching modes<sup>47,48</sup>. The bands at 1592 and 1370  $\text{cm}^{-1}$  can be assigned to the asymmetric and symmetric OCO stretching modes while that at 2868  $\text{cm}^{-1}$  is attributed to the CH stretching mode of the same species<sup>47,49,50</sup>. The  $^*\text{H}_3\text{CO}$  species is signalled by diagnostic modes at 2941 and 2838  $\text{cm}^{-1}$  that

are assigned to the CH<sub>3</sub> stretching modes and the band at 1182 cm<sup>-1</sup> is attributed to the CO stretching mode of bridged methoxide species<sup>47,48,51</sup>. In addition to \*HCOO and \*H<sub>3</sub>CO, \*CO<sub>2</sub> species were also observed, with bands at 1567 and 1379 cm<sup>-1</sup> that can be associated with the OCO stretching modes. Under light irradiation, all intermediates showed an increase in band intensity (Supplementary Fig. 19), thereby confirming the photochemical effect of CO<sub>2</sub> hydrogenation, and is consistent with the activity results. In the case of pristine In<sub>2</sub>O<sub>3</sub> (Fig. 5c and Supplementary Fig. 20), \*HCOO and \*H<sub>3</sub>CO species of virtually insignificant intensity were observed for CO<sub>2</sub> hydrogenation, and light irradiation resulted in much noisier peaks. This further indicates the moderate catalytic performance of pristine In<sub>2</sub>O<sub>3</sub> and the significant promotion effect resulting from single-site Bi<sup>3+</sup> substitution.

In summary, we have demonstrated a one-step solvothermal route towards atom-precise isomorphic substitution of In<sup>3+</sup> in In<sub>2</sub>O<sub>3</sub> by Bi<sup>3+</sup> to generate Bi<sub>x</sub>In<sub>2-x</sub>O<sub>3</sub> materials with full-spectrum UV-Vis-NIR absorption. The incorporation of single-site Bi atoms in the In<sub>2</sub>O<sub>3</sub> host lattice provides strong Lewis acid-base Bi<sup>3+</sup>-O<sup>2-</sup> pairs to enhance CO<sub>2</sub> adsorption and activation, resulting in distinctly enhanced reaction rates relative to those observed for pristine In<sub>2</sub>O<sub>3</sub> and other indium oxide based catalysts. The Bi 6s<sup>2</sup> lone pairs create mid-gap energy states, which can increase the harvesting of solar photons and favour the generation and separation of photo-induced charge carriers. Remarkably, single-site Bi<sup>3+</sup>-substituted Bi<sub>x</sub>In<sub>2-x</sub>O<sub>3</sub> proves to be a highly efficient and stable photocatalyst, achieving an impressive CO production rate *three orders of magnitude* greater than that of pristine In<sub>2</sub>O<sub>3</sub>, with notable photoactivity towards solar methanol. In addition to increased activity catalytic sites, the greening of indium oxide by single-site bismuth atom substitution represents a new approach to CO<sub>2</sub> photocatalyst engineering and is a further step towards the vision of a solar CO<sub>2</sub> refinery.

## Methods

**Synthesis of In<sub>2</sub>O<sub>3</sub> and Bi<sub>x</sub>In<sub>2-x</sub>O<sub>3</sub>.** Pristine In<sub>2</sub>O<sub>3</sub> nanocrystals were prepared via a simple solvothermal route. In a typical synthesis, 0.3 g of In(NO<sub>3</sub>)<sub>3</sub>·4.5H<sub>2</sub>O was dissolved in 17 mL [anhydrous DMF](#) solution. After stirring for 30 min, the obtained homogeneous solution was transferred into a Teflon-lined stainless steel autoclave and then heated at 150 °C for 24 hours. After being cooled to room temperature, the light-yellow product was collected through centrifugation, washed with ethanol and water, and finally dried at 60 °C in vacuum. Bi<sup>3+</sup>-substituted In<sub>2</sub>O<sub>3</sub> nanocrystals were prepared using the same method employed for pristine In<sub>2</sub>O<sub>3</sub>, except that various amounts of Bi(NO<sub>3</sub>)<sub>3</sub>·5H<sub>2</sub>O were added to the indium solution prior to solvothermal reaction.

**Material characterizations.** The content of Bi in  $\text{Bi}_x\text{In}_{2-x}\text{O}_3$  was determined using an inductively coupled plasma mass spectroscopy (ICP-MS) instrument (Optima 7300 DV). Powder X-ray diffraction (PXRD) was performed on a Bruker D2-Phaser X-ray diffractometer, using Cu K $\alpha$  radiation at 30 kV. X-ray photoelectron spectroscopy (XPS) was performed using a PerkinElmer Phi 5500 ESCA spectrometer in an ultrahigh vacuum chamber with a base pressure of  $1 \times 10^{-9}$  Torr. The spectrometer used an Al K $\alpha$  X-ray source operating at 15 kV and 27 mA. The samples were coated onto carbon tape prior to analysis and all results were calibrated to C1s 284.5 eV. EPR spectra were obtained at room temperature and 77 K using a Bruker A-300-EPR X-band spectrometer. Transmission electron microscopy (TEM) measurements were conducted using a JEM-2010 microscope working at 200 kV. The double spherical aberration-corrected scanning transmission electron microscope (STEM) images were obtained on an FEI Themis Z instrument. X-ray absorption spectra were collected at the BL14W beamline of the Shanghai Synchrotron Radiation Facility (SSRF). The storage ring of the SSRF was operated at 3.5 GeV with a stable current of 200 mA. Using a Si(111) double-crystal monochromator, the data collection was carried out in fluorescence mode using Lytle detector. All spectra were collected under ambient conditions. Diffuse reflectance spectra (DRS) of the powders were obtained for dry-pressed disk samples using a Cary 500 Scan Spectrophotometer (Varian, USA) over a range of 200 to 800 nm. Barium sulfate ( $\text{BaSO}_4$ ) was used as a reflectance standard. Room-temperature photoluminescence (PL) spectra were measured on an FL/FS 920 (Edinburgh Instruments) system equipped with a 450 W Xe arc lamp as the excitation source and a red sensitive Peltier element-cooled Hamamatsu R2658 PMT as the detector. Time-resolved fluorescence decay spectra were recorded on the Delta Pro (HORIBA instruments) using a 357 nm laser as the excitation source. BET surface area analyses were performed on an ASAP2020 M apparatus (Micromeritics Instrument Corp., USA) with the samples degassing in vacuum at 110 °C for 10 h and then measuring at 77 K. The  $\text{CO}_2$  temperature-programmed desorption ( $\text{CO}_2$ -TPD) measurements were carried out on AutoChem II 2920 Version. The density functional theory (DFT) calculations were performed using the Cambridge Sequential Total Energy Package (CASTEP) computational codes. During the geometry optimization, lattice parameters and atomic positions were optimized simultaneously. Based on the experimental data, we replaced one In with Bi in the cell as the  $\text{In}_{15}\text{BiO}_{24}$  model and deleted one of the oxygen atom that were coordinating with Bi to establish one  $\text{In}_{15}\text{BiO}_{23}(\text{O}_{\text{Vacancy}})$  model. For calculating the electronic structures and density of states, the geometry optimization of  $\text{In}_2\text{O}_3$  and  $\text{In}_{15}\text{BiO}_{23}(\text{O}_{\text{Vacancy}})$  were calculated by the PBE method within Generalized Gradient-corrected Approximation (GGA), using the exchange-correlation potential. The Vanderbilt ultrasoft pseudopotential with a cutoff energy of 380 eV was used to ensure the precision of the results. Brillouin zone integration was represented using the K-point sampling scheme of  $3 \times 3 \times 3$  Monkhorst-Pack scheme. The convergence tolerance for geometry optimization was selected with the differences in total energy ( $5.0 \times 10^{-6}$  eV/atom), the maximal ionic Hellmann-Feynman force ( $1.0 \times 10^{-2}$  eV/Å), the stress tensor ( $2.0 \times 10^{-2}$  GPa), and the maximal displacement ( $5.0 \times 10^{-4}$  Å).

Gas phase  $\text{CO}_2$  hydrogenation tests. Batch reactions were conducted in a custom-built 1.5 mL stainless steel batch reactor with a fused-silica viewport sealed with Viton O-rings. The reactor was evacuated

using an Alcatel dry pump prior to being purged with the reactant high-purity H<sub>2</sub> reactant gas. After purging the reactor, it was filled with a 1:1 stoichiometric mixture of H<sub>2</sub> (99.9995%) and CO<sub>2</sub> (99.999%) until the total pressure reached 30 psi. The reactor were irradiated with a 300 W Xe lamp for a duration of 1 h without external heating. Product gases were analyzed using flame ionization and thermal conductivity detectors installed in a SRI-8610 gas chromatograph equipped with 3 in. Mole Sieve 13a and 6 in. Haysep D column. Isotopically labeled tracing experiments were performed using <sup>13</sup>CO<sub>2</sub> (99.9 at%, Sigma-Aldrich). Isotope distributions in the product gases were measured using an Agilent 7890A gas chromatograph-mass spectrometer with a 60 m GS-carbon plot column leading to the mass spectrometer. Flow experiments were carried out in a fixed-bed tubular reactor with the catalyst material being packed into a quartz tube and immobilized at both ends with quartz wool. The quartz tube had an inner diameter of 2 mm with a wall thickness of 0.5 mm, and was placed into a groove carved out into a copper block. An OMEGA temperature controller was attached to two heating cartridges inserted into the copper block and a thermocouple was inserted into the quartz tube contacting the catalyst but covered by the quartz wool. A 300 W Xe arc lamp illuminated the catalyst plug at a measured intensity of 2 W cm<sup>-2</sup>. CO<sub>2</sub> and H<sub>2</sub> were flowed through with a 1 : 3 ratio (1 sccm CO<sub>2</sub>, 3 sccm H<sub>2</sub>). The amounts of CO and CH<sub>3</sub>OH produced were determined using gas chromatography-mass spectrometry (GC-MS, 7890B and 5977A, Agilent) using an He carrier gas.

***In-situ* DRIFT studies.** The in-situ DRIFTS measurements were performed to detect the surface intermediates over pristine In<sub>2</sub>O<sub>3</sub> and Bi<sub>x</sub>In<sub>2-x</sub>O<sub>3</sub> nanocrystals under reaction conditions. The spectra were collected using a Fourier-transform infrared spectroscopy spectrometer (Thermo, Nicolet 6700) equipped with an MCT detector. Before measurement, the catalyst was purged with He at 250 °C for 2 h. The catalyst was subsequently cooled down to 230 °C. The background spectrum with a resolution of 4 cm<sup>-1</sup> was obtained at 230 °C in He flow. Then the catalyst was exposed to a mixture of CO<sub>2</sub>, H<sub>2</sub>, and He (1 sccm CO<sub>2</sub>, 3 sccm H<sub>2</sub>, and 16 sccm He, respectively) in dark and light conditions for different times. The in-situ DRIFT spectra were recorded by collecting 32 scans at 4 cm<sup>-1</sup> resolution.

## Declarations

## Acknowledgments

T.Y. is thankful for financial support from the National Natural Science Foundation of China (21872081), Qingchuang Science and Technology of Shandong Province (2020KJC010). GAO acknowledges the financial support of the Ontario Ministry of Research and Innovation (MRI), the Ministry of Economic Development, Employment and Infrastructure (MEDI), the Ministry of the Environment and Climate Change's (MOECC) and the Best in Science (BIS) Award. Also acknowledged is additional support from the Ontario Center of Excellence (OCE) Solutions 2030 Challenge Fund, the Low Carbon Innovation Fund (LCIF), Imperial Oil, the University of Toronto Connaught Innovation Fund (CIF), the Connaught Global

Challenge (CGC) Fund, and the Natural Sciences and Engineering Research Council of Canada (NSERC). P.N.D. acknowledges personal funding providing by the NSERC PDF program.

## Author contributions

T.Y. and G.A.O. conceived and designed the experiments. T.Y., N.L. and L.L.Wang prepared the materials for characterizations. T.Y. and N.T. carried out the batch and flow experiments for CO<sub>2</sub> methanation. W.R. and N.L. carried out the DFT calculation. T.Y. performed the *in-situ* DRIFTS study and CO<sub>2</sub>-TPD test. L.Wang. performed the XPS characterization. M.X. and L.L.W. carried out the ICP-AES study. T.Y and L.L.Wan performed the MS test using <sup>13</sup>C. P.D. performed the XAFS XANES experiments. T.Y., N.L. and G.A.O. co-wrote the manuscript. All authors discussed the results and commented on the manuscript.

## Additional information

Supplementary information is available in the [online version of the paper](#). Reprints and permissions information is available online at [www.nature.com/reprints](http://www.nature.com/reprints). Correspondence and requests for materials should be addressed to T.Y. and G.A.O.

## Competing financial interests

The authors declare no competing financial interests.

## References

1. Dang, S. S., Qin, B., Yang, Y., Wang, H., Cai, J., Han, Y., Li, S. G., Gao, P. & Sun, Y. H. Rationally designed indium oxide catalysts for CO<sub>2</sub> hydrogenation to methanol with high activity and selectivity. *Adv.* **6**, eaaz2060 (2020).
2. Wang, M., Shen, M., Jin, X. X., Tian, J. J., Li, M. L., Zhou, Y. J., Zhang, L. X., Li, Y. S. & Shi, J. L. Oxygen vacancy generation and stabilization in CeO<sub>2-x</sub> by Cu introduction with improved CO<sub>2</sub> photocatalytic reduction activity. *ACS Catal.* **9**, 4573-4581 (2019).
3. Wang, W., Wang, S. P., Ma, X. B. & Gong, J. L. Recent advances in catalytic hydrogenation of carbon dioxide. *Soc. Rev.* **40**, 3703-3727 (2011).
4. Jia, J., O'Brien, P. G., He, L., Qiao, Q., Fei, T., Reyes, L. M., Burrow, T. E., Dong, Y. C., Liao, K., Varela, M., Pennycook, S. J., Hmadeh, M., Helmy, A. S., Kherani, N. P., Perovic, D. D. & G. A. Ozin, Visible and near-infrared photothermal catalyzed hydrogenation of gaseous CO<sub>2</sub> over nanostructured Pd@Nb<sub>2</sub>O<sub>5</sub>. *Sci.* **3**, 1600189 (2016).

5. Meng, X. G., Wang, T., Liu, L. Q., Ouyang, S. X., Li, P., Hu, H. L., Kako, T., Iwai, H., Tanaka A. & Ye, J. H. Photothermal conversion of CO<sub>2</sub> into CH<sub>4</sub> with H<sub>2</sub> over group VIII nanocatalysts: An alternative approach for solar fuel production. *Chem. Int. Ed.* **53**, 11478-11482 (2014).
6. Chen, G. B., Gao, R., Zhao, Y. F., Li, Z. H., Waterhouse, G. I. N., Shi, R., Zhao, J. Q., Zhang, M. T., Shang, L., Sheng, G. Y., Zhang, X. P., Wen, X. D., Wu, Z., Tung, C. H. & Zhang, T. R. Alumina-supported CoFe alloy catalysts derived from layered-double-hydroxide nanosheets for efficient photothermal CO<sub>2</sub> hydrogenation to hydrocarbons. *Adv. Mater.* **29**, 1704663 (2017).
7. Feng, K., Wang, S. H., Zhang, D. K., Wang, L., Yu, Y. Y., Feng, K., Li, Z., Zhu, Z. J., Li, C. R., Cai, M. J., Wu, Z. Y., Kong, N., Yan, B. H., Zhong, J., Zhang, X. H., Ozin, G. A. & He, L. Cobalt plasmonic superstructures enable almost 100% broadband photon efficient CO<sub>2</sub> *Adv. Mater.* **32**, 2000014 (2020).
8. Stephan, D. W. Frustrated Lewis pairs. *Am. Chem. Soc.* **137**, 10018-10032 (2015).
9. Stephan, D. W. & Erker, G. Frustrated Lewis pair chemistry: Development and perspectives. *Chem. Int. Ed.* **54**, 6400-6441 (2015).
10. Ma, Y. Y., Zhang, S., Chang, C. R., Huang, Z. Q., Ho, J. C. & Qu, Y. Q. Semi-solid and solid frustrated Lewis pair catalysts. *Soc. Rev.* **47**, 5541-5553 (2018).
11. Ghuman, K. K., Wood, T. E., Hoch, L. B., Mims, C. A., Ozin, G. A. & Singh, C. V. Illuminating CO<sub>2</sub> reduction on frustrated Lewis pair surfaces: investigating the role of surface hydroxides and oxygen vacancies on nanocrystalline In<sub>2</sub>O<sub>3-x</sub>(OH)<sub>y</sub>. *Chem. Chem. Phys.* **17**, 14623-14635 (2015).
12. Yan, T., Wang, L., Liang, Y., Makaremi, M., Wood, T.E., Dai, Y., Huang, B. B., Jelle, A. A., Dong, Y.C. & Ozin, G. A. Polymorph selection towards photocatalytic gaseous CO<sub>2</sub> hydrogenation. *Nat. Commun.* **10**, 2521-2530 (2019).
13. Wang, , Yan, T. J., Song, R., Sun, W., Guo, J. L., Zhang, Z. Z., Wang, X. X. & Ozin, G. A. Room-temperature activation of H<sub>2</sub> by a surface frustrated Lewis pair. *Angew. Chem. Int. Ed.* **58**, 9501-9505 (2019).
14. Wang, X. H., Lu, L., Wang, B., Xu, Z., Xin, Z. Y., Yan, S. C., Geng, R. & Zou, Z. G. Frustrated Lewis pairs accelerating CO<sub>2</sub> reduction on oxyhydroxide photocatalysts with surface lattice hydroxyls as a solid-state proton donor. *Adv. Funct. Mater.* **28**, 1804191-1804199 (2018).
15. Zhang, S., Huang, Q., Ma, Y. Y., Gao, W., Li, W., Cao, F. X., Li, L., Chang, C. R. & Qu, Y. Q. Solid frustrated-Lewis-pair catalysts constructed by regulations on surface defects of porous nanorods of CeO<sub>2</sub>. *Nat. Commun.* **8**, 15266-15277 (2017).
16. Wang, J. Y., Liu, C. Y., Senftle, T. P., Zhu, J., Zhang, G. H., Guo, X. W. & Song, C. S. Variation in the In<sub>2</sub>O<sub>3</sub> crystal phase alters catalytic performance toward the reverse water gas shift reaction. *ACS Catal.* **10**, 3264-3273 (2020).
17. Wang, L. R., Cai, J. Y., Xie, Y. C. Z., Guo, J. S., Xu, L. X., Yu, S. Y., Zheng, X. S., Ye, J., Zhu, J. F., Zhang, L. J., Liang, S. Q. & Wang, L. B. In<sub>2</sub>O<sub>3</sub> nanocrystals for CO<sub>2</sub> fixation: Atomic-level insight into the role of grain boundaries. *iScience* **16**, 390-398 (2019).

18. Sun, K. H., Fan, Z. G., Ye, J. Y., Yan, J. M., Ge, Q. F., Li, Y. N., He, W. J., Yang, W. M. & Liu, C. J. Hydrogenation of CO<sub>2</sub> to methanol over In<sub>2</sub>O<sub>3</sub> *J. CO<sub>2</sub> Utilization* **12**, 1-6 (2015).
19. Ye, J. Y., Liu, C. J., Mei, D. H. & Ge, Q. F. Active oxygen vacancy site for methanol synthesis from CO<sub>2</sub> hydrogenation on In<sub>2</sub>O<sub>3</sub>(110): A DFT study. *ACS Catal.* **3**, 1296-1306 (2013).
20. Ye, J. Y., Liu, C. J. & Ge, Q. F. DFT study of CO<sub>2</sub> adsorption and hydrogenation on the In<sub>2</sub>O<sub>3</sub> *J. Phys. Chem. C* **116**, 7817-7825 (2012).
21. Martin, O., Martín, A. J., Mondelli, C., Mitchell, S., Segawa, T. F., Hauert, R., Drouilly, C., Ferré, D. C. & Ramírez, J. P. Indium oxide as a superior catalyst for methanol synthesis by CO<sub>2</sub> *Angew. Chem. Int. Ed.* **55**, 6261-6265 (2016).
22. Gao, P., Li, S. G., Bu, X. M., Dang, S. S., Liu, Z. Y., Wang, H., Zhong, L. S., Qiu, M. H., Yang, C. G., Cai, J., Wei, W. & Sun, Y. H. Direct conversion of CO<sub>2</sub> into liquid fuels with high selectivity over a bifunctional catalyst. *Chem.* **9**, 1019-1024 (2017).
23. Wang, L., Dong, Y. C., Yan, T. J., Hu, Z. X., Jelle, A. A., Meira, D. M., Duchesne, P. N., Loh, J. Y. Y., Qiu, C. Y., Storey, E. E., Xu, Y. F., Sun, W., Ghossoub, M., Kherani, N. P., Helmy, A. S. & Ozin, G. A. Black indium oxide a photothermal CO<sub>2</sub> hydrogenation catalyst. *Commun.* **11**, 2432-2439 (2020).
24. Frei, M. S., Mondelli, C., Muelas, R. G., Kley, K. S., Puértolas, B., López, N., Safonova, O. V., Stewart, J. A., Ferré, D. C. & Ramírez, J. P. Atomic-scale engineering of indium oxide promotion by palladium for methanol production via CO<sub>2</sub> *Nat. Commun.* **10**, 3377-3387 (2019).
25. Mohan, Green bismuth. *Nat. Chem.* **2**, 336-336 (2010).
26. Gordon, R. & Rutledge, J. W. Bismuth bronze from Machu Picchu, Peru. *Science* **223**, 585-586 (1984).
27. Rohr, Bismuth-the new ecologically green metal for modern lubricating engineering. *Ind. Lubr. Tribol.* **54**, 153-164 (2002).
28. Leng, M., Chen, Z. W., Yang, Y., Li, Z., Zeng, K., Li, K. H., Niu, G. D., He, Y. S., Zhou, Q. C. & Tang, J. Lead-free, blue emitting bismuth halide perovskite quantum dots. *Angew. Chem. Int. Ed.* **55**, 1-6 (2016).
29. Ye, Q., Deng, Y., Wang, L., Xie, H. Q. & Su, F. Y. Bismuth-based photocatalysts for solar photocatalytic carbon dioxide Conversion. *ChemSusChem* **12**, 3671-3701 (2019).
30. Dong, C., Ghuman, K. K., Popescu, R., Duchesne, P. N., Zhou, W. J., Loh, J. Y. Y., Jelle, A. A., Jia, J., Wang, D., Mu, X. K., Kübel, C., Wang, L., He, L., Ghossoub, M., Wang, Q., Wood, T. E., Reyes, L. M., Zhang, P., Kherani, N. P., Singh, C. V. & Ozin, G. A. Tailoring surface frustrated Lewis pairs of In<sub>2</sub>O<sub>3-x</sub>(OH)<sub>y</sub> for gas-phase heterogeneous photocatalytic reduction of CO<sub>2</sub> by isomorphous substitution of In<sup>3+</sup> with Bi<sup>3+</sup>. *Adv. Sci.* **5**, 1700732-1700742 (2018).
31. Ghossoub, M., Xia, M., Duchesne, P. N., Segal, D. & Ozin, G. A. Principles of photothermal gas-phase heterogeneous CO<sub>2</sub> catalysis. *Energ. Environ. Sci.* **12**, 1122-1142 (2019).
32. Kanhere, D., Zheng, J. W. & Chen, Z. Site specific optical and photocatalytic properties of Bi-doped NaTaO<sub>3</sub>. *J. Phys. Chem. C* **115**, 11846-11853 (2011).

33. Mizoguchi, H., Ueda, K., Kawazoe, , Hosono, H., Omata, T., Fujitsu, S. New mixed-valence oxides of bismuth:  $\text{Bi}_{1-x}\text{Y}_x\text{O}_{1.5+d}$  ( $x=0.4$ ). *J. Mater. Chem.* **7**, 943-946 (1997).
34. Liang, C. , Meng, G. W., Lei, Y., Phillipp, F. & Zhang, L. D. Catalytic growth of semiconducting  $\text{In}_2\text{O}_3$  nanofibers. *Adv. Mater.* **13**, 1330-1333 (2001).
35. Saison, T., Chemin, N., Chanéac, , Durupthy, O., Ruaux, V., Mariey, L., Mangé, F., Beaunier, P., Jolivet, J. P.  $\text{Bi}_2\text{O}_3$ ,  $\text{BiVO}_4$ , and  $\text{Bi}_2\text{WO}_6$ : Impact of surface properties on photocatalytic activity under visible light. *J. Phys. Chem. C* **115**, 5657-5666 (2011).
36. Lei, F. C., Sun, Y. F. Liu, K. T., Gao, S., Liang, L., Pan, B. C. & Xie, Y. Oxygen vacancies confined in ultrathin indium oxide porous sheets for promoted visible-light water splitting. *Am. Chem. Soc.* **136**, 6826-6829 (2014).
37. Hoch, L. B., Szymanski, P., Ghuman, K. K., He, L., Liao, K., Qiao, Q., Reyes, L. M., Zhu, Y. M., El-Sayed, M. A., Singh, C. V. & Ozin, G. A. Carrier dynamics and the role of surface defects: Designing a photocatalyst for gas-phase  $\text{CO}_2$  *Proc. Natl. Acad. Sci. USA* **113**, E8011- E8020 (2016).
38. Hao, X. , Zhou, J., Cui, Z. W., Wang, Y. Y., Wang, Y. & Zou, Z. G. Zn-vacancy mediated electron-hole separation in  $\text{ZnS/g-C}_3\text{N}_4$  heterojunction for efficient visible-light photocatalytic hydrogen production. *Appl. Catal. B* **229**, 41-51 (2018).
39. Lu, Y. , Lin, W. H., Yang, C. Y., Chiu, Y. H., Pu, Y. C., Lee, M. H., Tseng, Y. C. & Hsu, Y. J. A facile green antisolvent approach to  $\text{Cu}^{2+}$ -doped  $\text{ZnO}$  nanocrystals with visible-light-responsive Photoactivities. *Nanoscale* **6**, 8796-8803 (2014).
40. Dong, F., Zhao, Z. W., Sun, Y. J., Zhang, Y. X., Yan, S. & Wu, Z. B. An advanced semimetal-organic Bi spheres/ $\text{g-C}_3\text{N}_4$  nanohybrid with SPR enhanced visible-light photocatalytic performance for NO purification. *Sci. Technol.* **49**, 12432-12440 (2015).
41. Wang, , Zhao, J., Wang, T. F., Li, Y. X., Li, X. Y., Yin, J. & Wang, C. Y.  $\text{CO}_2$  photoreduction with  $\text{H}_2\text{O}$  vapor on highly dispersed  $\text{CeO}_2/\text{TiO}_2$  catalysts: Surface species and their reactivity. *J. Catal.* **337**, 293-302 (2016).
42. Jia, J., Qian, C. X., Dong, Y. C., Li, Y. F., Wang, H., Ghossoub, M., Butler, K. T., Walsh, A. & Ozin, G. A. Heterogeneous catalytic hydrogenation of  $\text{CO}_2$  by metal oxides: defect engineering – perfecting Imperfection. *Soc. Rev.* **46**, 4631-4644 (2017).
43. Pokrovski, K., Jung, K. & Bell, A. T. Investigation of CO and  $\text{CO}_2$  adsorption on tetragonal and monoclinic zirconia. *Langmuir* **17**, 4297-4303 (2001).
44. Li, S. , Xu, Y., Chen, Y. F., Li, W. Z., Lin, L. L., Li, M. Z., Deng, Y. C., Wang, X. P., Ge, B. H., Yang, C., Yao, S. Y., Xie, J. L., Li, Y. W., Liu, X. & Ma, D. Tuning the selectivity of catalytic carbon dioxide hydrogenation over iridium/cerium oxide catalysts with a strong metal–support interaction. *Angew. Chem. Int. Ed.* **56**, 10761-10765 (2017).
45. Luo, C., Zhao, J., Li, Y. , Zhao, W., Zeng, Y. B., Wang, C. Y. Photocatalytic  $\text{CO}_2$  reduction over  $\text{SrTiO}_3$ : Correlation between surface structure and activity. *Appl. Surf. Sci.* **447**, 627-635 (2018).

46. Walsh, A. & Catlow, C. R. A. Structure, stability and work functions of the low index surfaces of pure indium oxide and Sn-doped indium oxide (ITO) from density functional theory. *Mater. Chem.* **20**, 10438-10444 (2010).
47. Kattel, S., Yan, B., Yang, , Chen, J. G., Liu, P. Optimizing binding energies of key intermediates for CO<sub>2</sub> hydrogenation to methanol over oxide-supported copper. *J. Am. Chem. Soc.* **138**, 12440-12450 (2016).
48. Fisher, A. & Bell, A. T. In-situ infrared study of methanol synthesis from H<sub>2</sub>/CO<sub>2</sub> over Cu/SiO<sub>2</sub> and Cu/ZrO<sub>2</sub>/SiO<sub>2</sub>. *J. Catal.* **172**, 222-237 (1997).
49. Bianchi, D., Chafik, T., Khalfallah, & Teichner, S. J. Intermediate species on zirconia supported methanol aerogel catalysts. IV. Adsorption of carbon dioxide. *Appl. Catal.* **105**, 219-235 (1994).
50. Guglielminotti, Infrared study of syngas adsorption on zirconia. *Langmuir* **6**, 1455-1460 (1990).
51. Rhodes, , Pokrovski, K. & Bell, A. The effects of zirconia morphology on methanol synthesis from CO and H<sub>2</sub> over Cu/ZrO<sub>2</sub> catalysts Part II. Transient-response infrared studies. *J. Catal.* **233**, 210-220 (2005).

## Figures

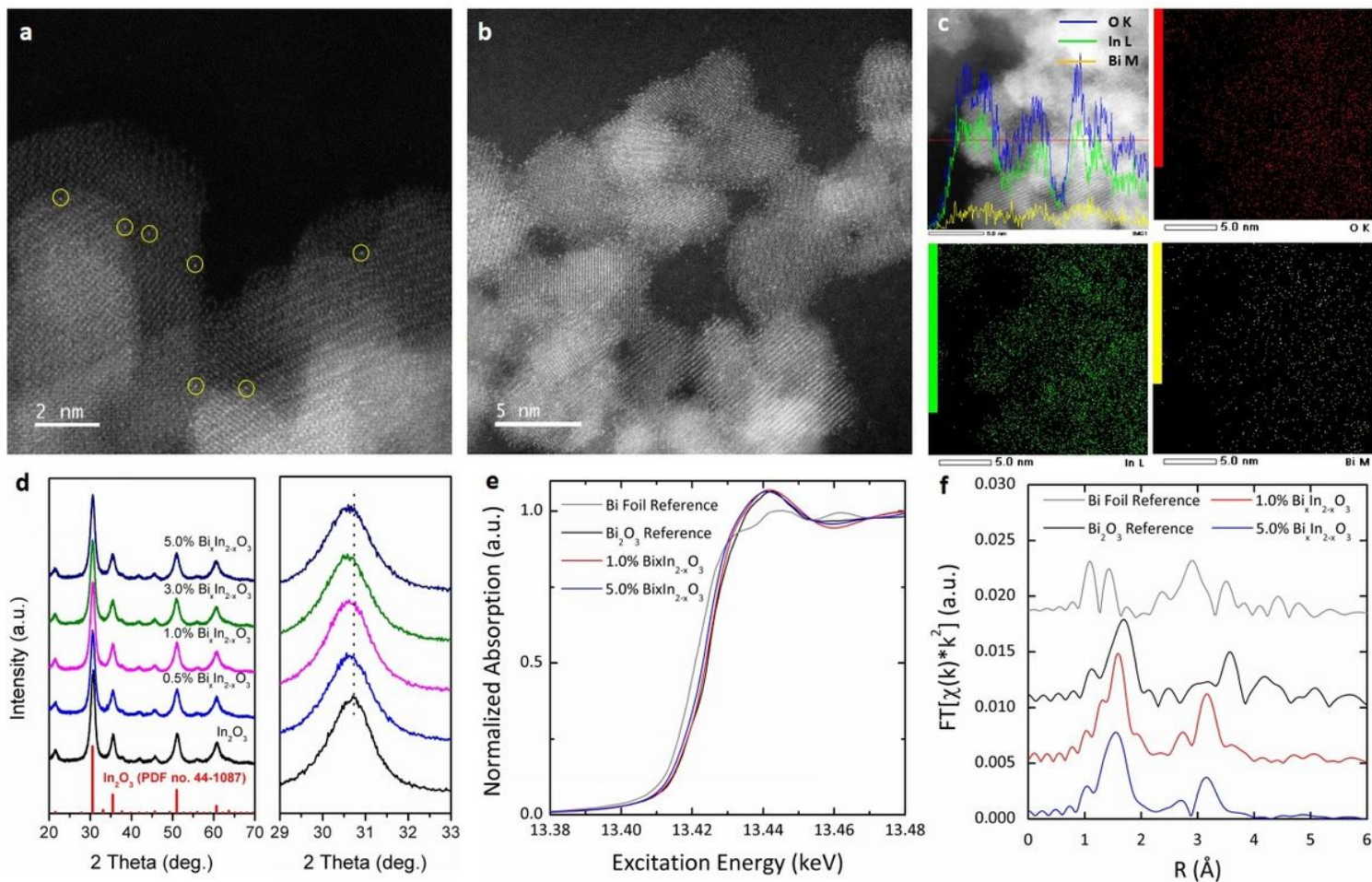


**Figure 1**

Structural characterizations of single-site Bi<sup>3+</sup> substituted BixIn<sub>2-x</sub>O<sub>3</sub>. a, Aberration-corrected STEM image of 1.0% BixIn<sub>2-x</sub>O<sub>3</sub> nanocrystals. b, Aberration-corrected STEM image of 5.0% BixIn<sub>2-x</sub>O<sub>3</sub> nanocrystals. c, EDS mapping profiles of 5.0% BixIn<sub>2-x</sub>O<sub>3</sub> along the indicated red line. d, PXRD patterns of BixIn<sub>2-x</sub>O<sub>3</sub> nanocrystals and pristine In<sub>2</sub>O<sub>3</sub>. e, Normalized Bi L<sub>3</sub>-edge XANES spectra of 1.0% and 5.0% BixIn<sub>2-x</sub>O<sub>3</sub> as well as Bi foil and Bi<sub>2</sub>O<sub>3</sub> references. f, k<sub>3</sub>-Weighted Bi L<sub>3</sub>-edge Fourier-transform EXAFS spectra of 1.0% and 5.0% BixIn<sub>2-x</sub>O<sub>3</sub> as well as Bi foil and Bi<sub>2</sub>O<sub>3</sub> references.

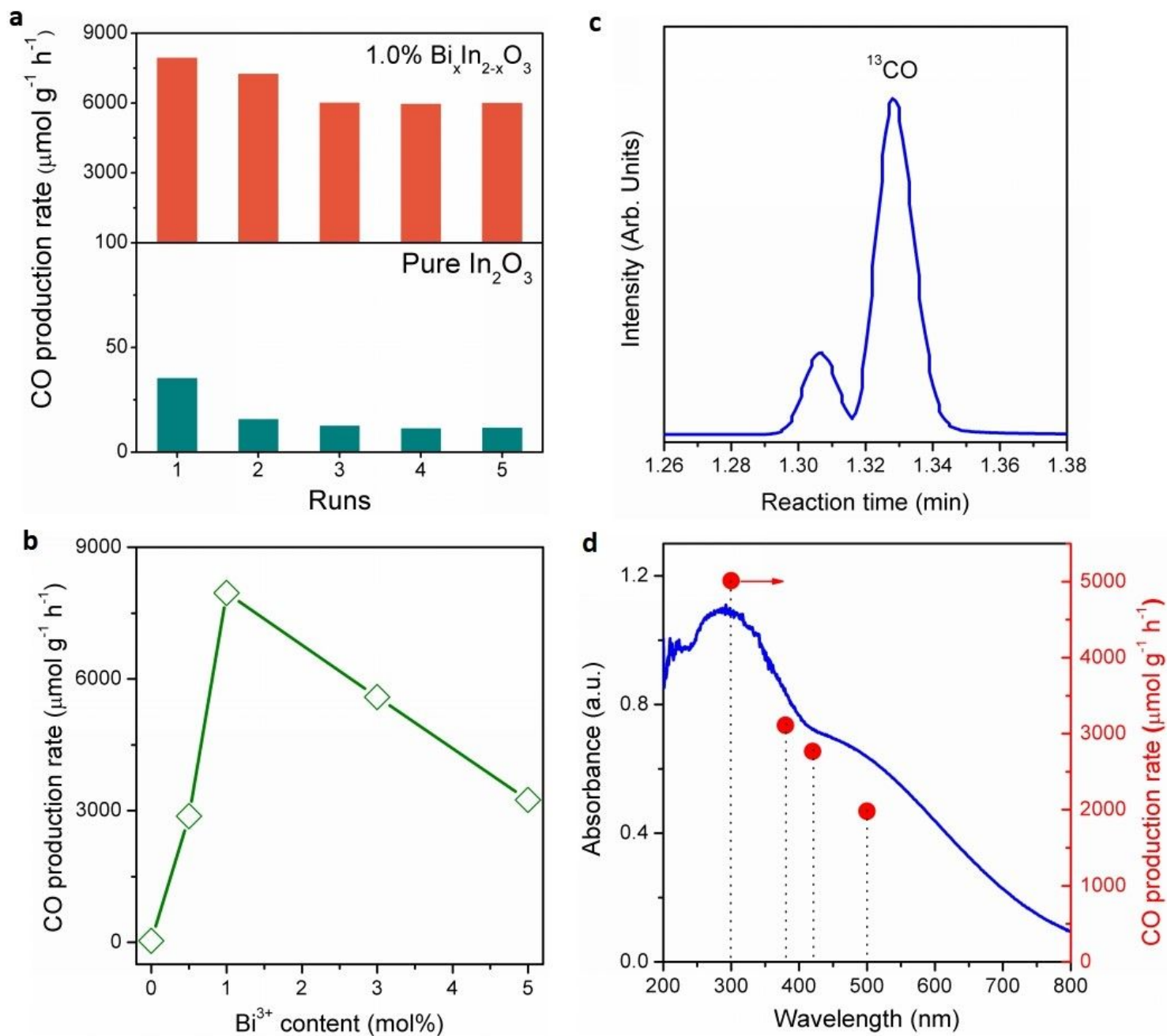


**Figure 2**

Photocatalytic performance in the batch reactor. a, CO rate of pristine In<sub>2</sub>O<sub>3</sub> (down) and 1.0% BiIn<sub>2-x</sub>O<sub>3</sub> nanocrystals (up) in catalyzing hydrogenation of CO<sub>2</sub> under illumination. b, CO rate as a function of Bi<sup>3+</sup> content for various BiIn<sub>2-x</sub>O<sub>3</sub> nanocrystals. c, GC-MS plot of <sup>13</sup>CO produced from <sup>13</sup>CO<sub>2</sub> over 1.0% BiIn<sub>2-x</sub>O<sub>3</sub> nanocrystals. d, CO rate as a function of absorption cut-off filter wavelength for 1.0% BiIn<sub>2-x</sub>O<sub>3</sub> nanocrystals.

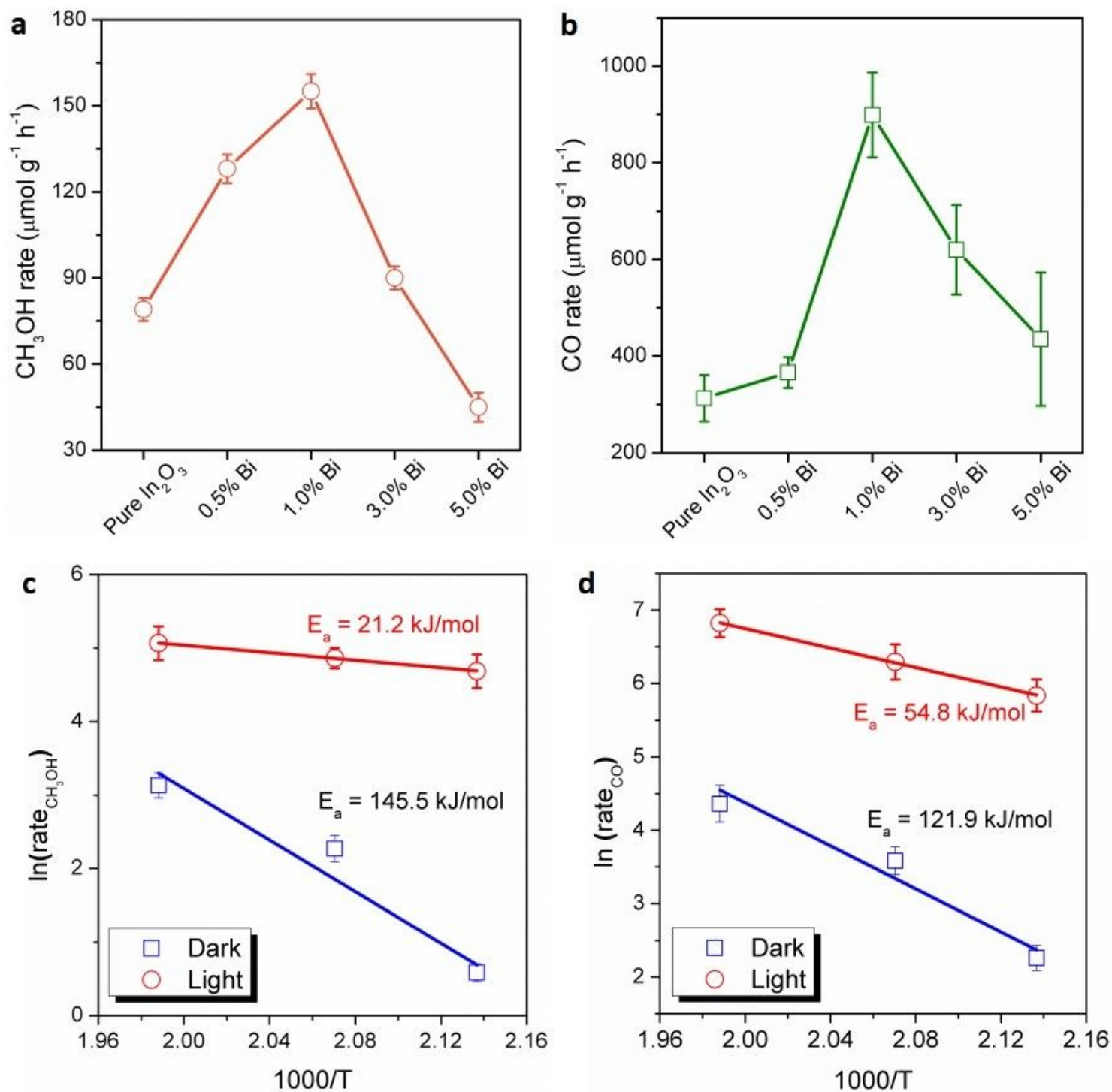


**Figure 3**

Catalytic performance in the flow reactor with and without light irradiation. a, CH<sub>3</sub>OH production rates as a function of Bi<sup>3+</sup> content under light irradiation and at 230 °C. b, CO production rates as a function of Bi<sup>3+</sup> content under light irradiation and at 230 °C. c, Arrhenius plots for CH<sub>3</sub>OH production rates of 1.0% Bi<sub>2</sub>O<sub>3</sub>In<sub>2</sub>-xO<sub>3</sub> with and without solar irradiation. d, Arrhenius plots for CO production rates of 1.0% Bi<sub>2</sub>O<sub>3</sub>In<sub>2</sub>-xO<sub>3</sub> with and without solar irradiation.

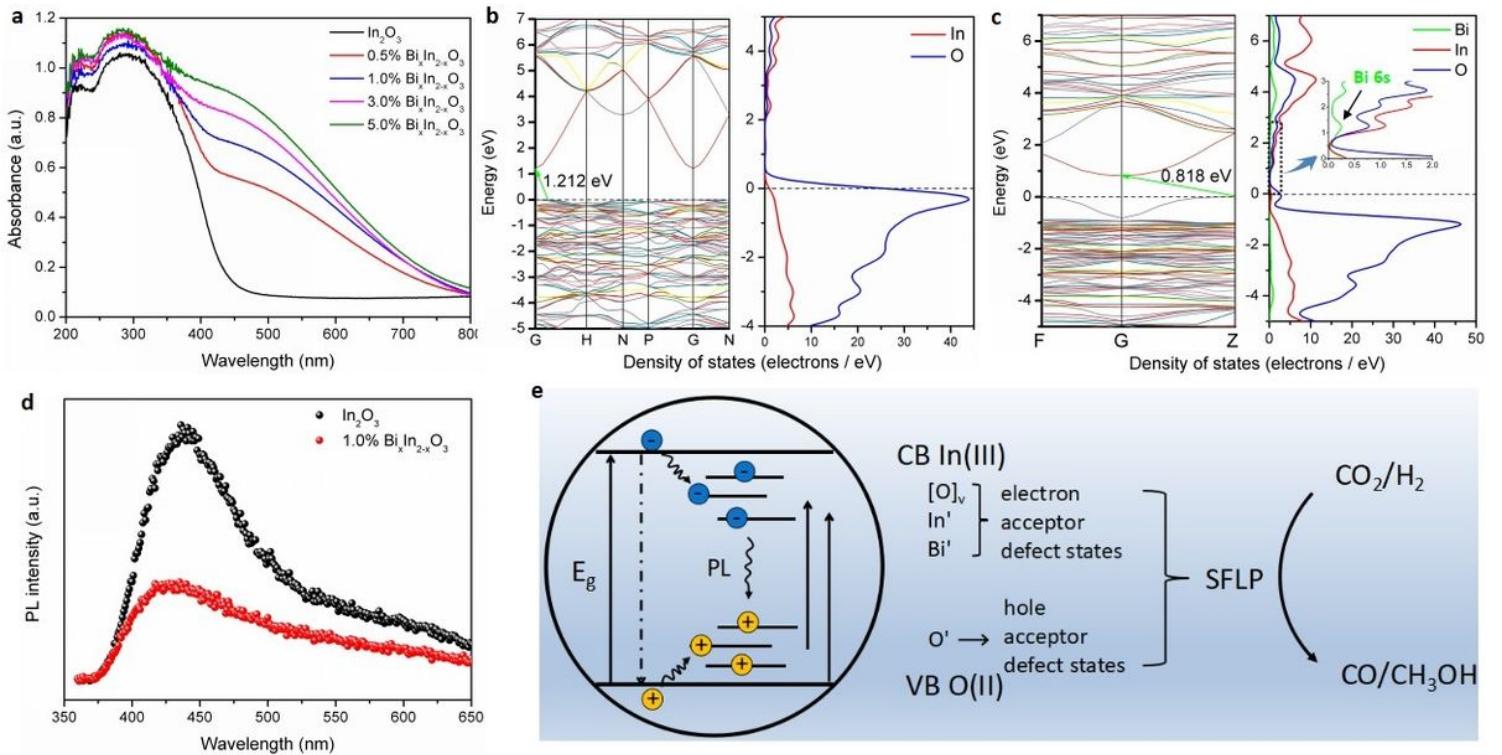


**Figure 4**

Electronic structures of  $\text{Bi}_x\text{In}_{2-x}\text{O}_3$ . a, Diffuse reflectance spectra of pristine  $\text{In}_2\text{O}_3$  and various  $\text{Bi}_x\text{In}_{2-x}\text{O}_3$  nanocrystals. b, The simulated band structure and DOS plots of pristine  $\text{In}_2\text{O}_3$ . c, The simulated band structure and DOS plots of  $\text{Bi}_x\text{In}_{2-x}\text{O}_3$  nanocrystals. d, Room-temperature PL spectra of pristine  $\text{In}_2\text{O}_3$  and 1.0%  $\text{Bi}_x\text{In}_{2-x}\text{O}_3$  nanocrystals using an excitation wavelength of 325 nm. e, Schematic illustrating charge carrier recombination pathways (SFLPs) and enabling  $\text{CO}_2$  hydrogenation reactions.

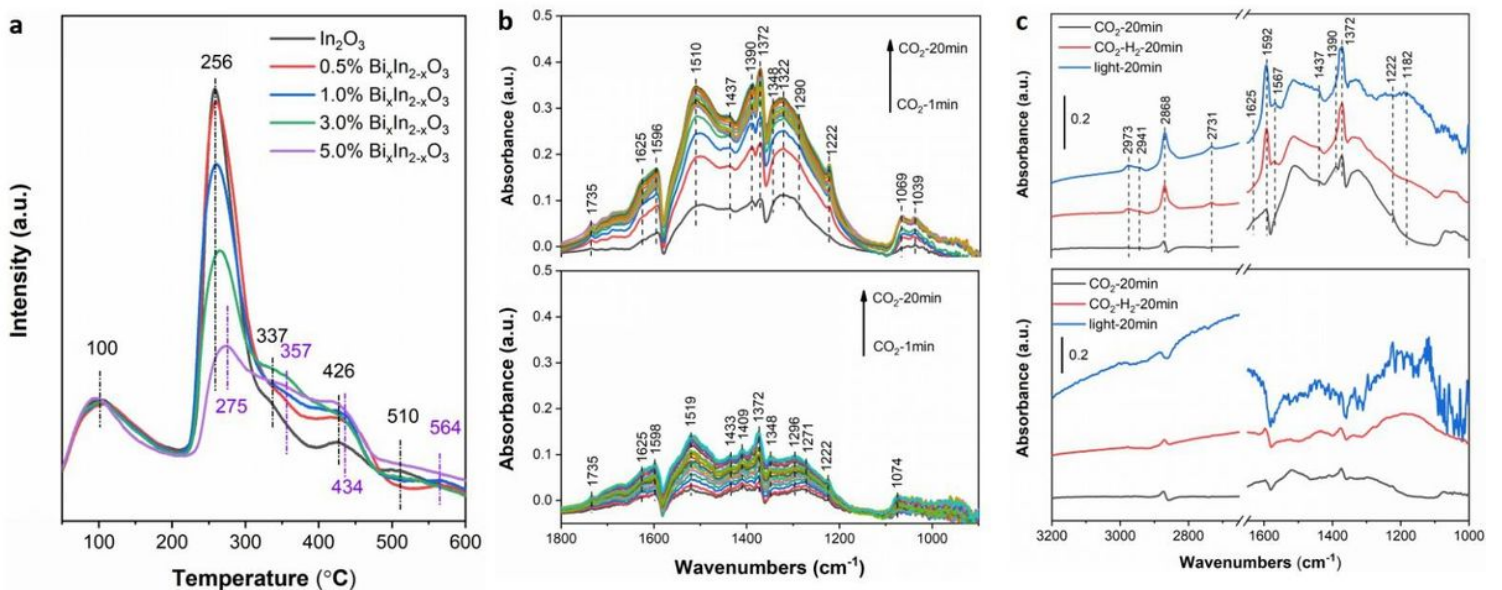


**Figure 5**

In-situ DRIFTS experiments of CO<sub>2</sub> adsorption and CO<sub>2</sub> hydrogenation. a, CO<sub>2</sub>-TPD profiles. b, In-situ DRIFTS spectra for the adsorption of CO<sub>2</sub> on 1.0% BiIn<sub>2-x</sub>O<sub>3</sub> nanocrystals (up) and pure In<sub>2</sub>O<sub>3</sub> (down). c, In-situ DRIFTS spectra of surface species under reaction conditions on 1.0% BiIn<sub>2-x</sub>O<sub>3</sub> nanocrystals (up) and pure In<sub>2</sub>O<sub>3</sub> (down).

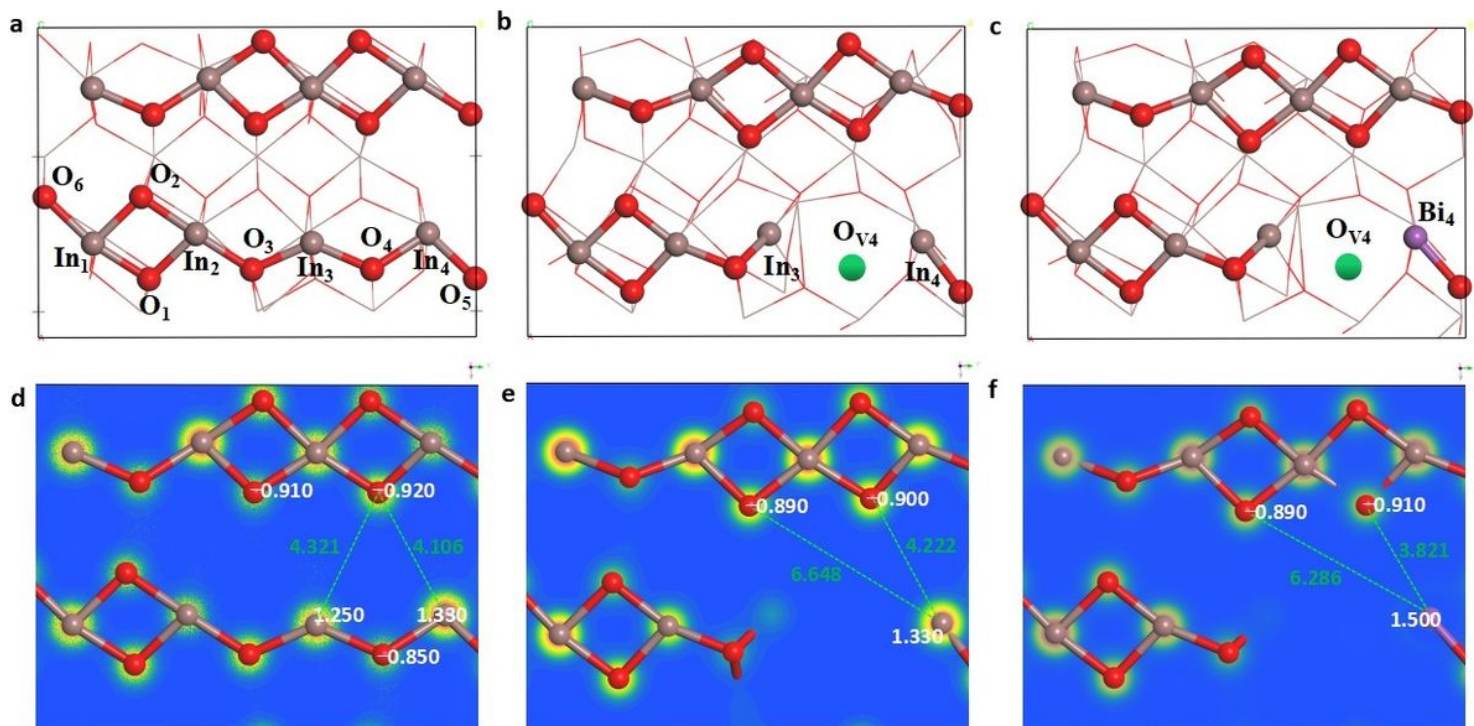


**Figure 6**

Schematic images of the reactivity of SFLPs in single-site Bi<sup>3+</sup> substituted BiIn<sub>2-x</sub>O<sub>3</sub>. a, Optimized structure of perfect In<sub>2</sub>O<sub>3</sub> (110). b, Optimized structure of defective In<sub>2</sub>O<sub>3</sub> (110) with one oxygen vacancy. c, Optimized structure of BiIn<sub>2-x</sub>O<sub>3</sub> (110) with Bi<sup>3+</sup> substitution. d, Electron-density isosurface of perfect In<sub>2</sub>O<sub>3</sub> (110). e, Electron-density isosurface of defective In<sub>2</sub>O<sub>3</sub> (110) with one oxygen vacancy. f, Electron-density isosurface of BiIn<sub>2-x</sub>O<sub>3</sub> (110) with Bi<sup>3+</sup> substitution.

## Supplementary Files

This is a list of supplementary files associated with this preprint. Click to download.

- [Supplementarymaterial.docx](#)
- [TableS1.png](#)
- [TableS2.png](#)
- [TableS3.png](#)
- [TableS4.png](#)
- [FigureS1.png](#)
- [FigureS2.jpg](#)

- FigureS3.jpg
- FigureS4.jpg
- FigureS5.jpg
- FigureS6.jpg
- FigureS7.png
- FigureS8.jpg
- FigureS9.jpg
- FigureS10.jpg
- FigureS11.jpg
- FigureS12.jpg
- FigureS13.jpg
- FigureS14.jpg
- FigureS15.jpg
- FigureS16.jpg
- FigureS17.jpg
- FigureS18.jpg
- FigureS19.jpg
- FigureS20.png